OPEN ACCESS

Influence of Conversion Time on Polymeric Speciation in Zirconium Conversion Coatings Deposited on Aluminium Alloy 5754: A ToF-SIMS Study

To cite this article: Ana Kraš *et al* 2026 *J. Electrochem. Soc.* **173** 071501

Journal of The Electrochemical Society, 2026 **173** 071501

Influence of Conversion Time on Polymeric Speciation in Zirconium Conversion Coatings Deposited on Aluminium Alloy 5754: A ToF-SIMS Study

Ana Kraš,[1,*] Ingrid Milošev,[1,*,z] Antoine Seyeux,[2] and Philippe Marcus[2,,z]**

[1]*Jožef Stefan Institute, Department of Physical and Organic Chemistry, Jamova c. 39, SI-1000 Ljubljana, Slovenia*
[2]*CNRS—Chimie ParisTech PSL University, Institut de Recherche de Chimie Paris, Physical Chemistry of Surfaces Group, Paris 75005, France*

The influence of conversion time on polymeric speciation and protective performance of zirconium conversion coatings (ZrCCs) on aluminium alloy AA5754 was investigated using samples treated in 150 ppm H_2ZrF_6 at pH 4.6 for 230 s and 480 s. Characterisation combined time-of-flight secondary ion mass spectrometry (ToF-SIMS) with region-of-interest analysis, electrochemical impedance spectroscopy in dilute Harrison's solution after one hour, atomic force microscopy, and contact-angle measurements. ZrCC thickening is conversion-time-dependent, with a preference for growth above intermetallic particles. ToF-SIMS identified monomeric, dimeric, and trimeric zirconium hydroxide fragments, while tetrameric species were detected only at very low intensities, in contrast to previous observations on steel, possibly due to the lower overall pH increase during ZrCC formation. Despite the thicker layer obtained at 480 s, EIS indicated no improvement in corrosion protection compared with the 230 s. Morphological and wettability analyses further showed that the shorter treatment produced a rougher but more compact and uniform coating, which correlates with better short-term protective behaviour. These findings emphasise that compactness and uniformity, rather than thickness or wettability, govern the early protective function of ZrCCs and raise the question of whether tetrameric polymeric forms are required to establish a protective layer, as hypothesised for cold-rolled steel.
 [DOI: 10.1149/1945-7111/ae54d6]

Manuscript submitted January 6, 2026; revised manuscript received March 18, 2026. Published March 31, 2026.

Supplementary material for this article is available online

Zirconium conversion coatings (ZrCCs) are increasingly considered environmentally sustainable alternatives to chromate- and phosphate-based systems. Their optimisation, however, requires a detailed understanding of zirconium aqueous chemistry,[1] which is complicated by extensive hydrolysis and the dynamic equilibrium of mono- and polymeric species.[2,3]

In our recent thermodynamic modelling of the Zr–OH and Zr–F systems, we elucidated speciation behaviour under coating-relevant conditions[1] and confirmed, via time-of-flight secondary ion mass spectrometry (ToF-SIMS),[4] the presence of tetrameric zirconium species within the amorphous oxide phase on cold-rolled steel—supporting Clearfield's early structural hypothesis for the Zr–OH system.[5]

On cold-rolled steel, ZrCC deposition proceeds along uniform corrosion of the substrate, resulting in homogeneous coatings, as demonstrated in our previous work.[6] To extend these insights, we now focus on aluminium alloys, specifically AA5754, a substrate widely used in the automotive industry and previously examined in another study[7] alongside cold-rolled steel and zinc. The aluminium alloy substrate differs from that of cold-rolled steel and zinc in the localised manner in which corrosion proceeds, namely, primarily around intermetallic particles (IMPs), which are electrochemically different from the matrix, leading to preferential growth of the ZrCC at the IMPs.

Interestingly, although ZrCCs and chromate conversion coatings (CCCs) deposited on aluminium alloys share a similar initiation mechanism—film nucleation at cathodic IMPs driven by galvanic coupling—their subsequent evolution diverges. In CCCs, reduction of Cr(VI) to Cr(III) produces a compact film that passivates IMPs, suppresses local cathodic activity, and shifts growth to the matrix, aided by matrix-side porosity, acting as an anodic inhibitor.[8,9] By contrast, ZrCCs lack such redox feedback, where hydrolysed Zr(IV) species condense rapidly, and deposition persists at IMPs even after the Volta potential difference between IMPs and the matrix has diminished.[8,10] This leads to widely observed preferential thickening, stress accumulation, and cracking above IMPs. In terms of blocking cathodic sites, ZrCCs act more as cathodic inhibitors, at least at the initial stage of immersion in an aggressive solution.[7,8,11–16]

Response Surface Methodology (RSM) on AA5754 pinpointed that lower concentrations and shorter conversion times were required due to the dominant role of cathodic IMPs.[7] Optimal deposition was achieved at 150 ppm H_2ZrF_6, pH 4.6, with a 230 s conversion time, producing coatings with minimal Zr content differences between the matrix and IMPs, as confirmed by scanning electron microscopy with energy dispersive X-ray spectroscopy (SEM/EDS). We thus hypothesised[7] that employing these conditions—being closer to the zirconia precipitation threshold—would favour a more chemically driven rather than electrochemically driven process,[1] thereby reducing differences in ZrCC deposition between IMPs and the aluminium matrix.[7]

Short-term (after 1 h of immersion) electrochemical impedance spectroscopy (EIS) analysis recorded in dilute Harrison's solution further suggested that longer conversion times (up to 480 s) under the same conditions could improve corrosion resistance. However, extended deposition increased the risk of cracking at IMPs, likely due to overgrowth and stress accumulation.[7] Prior studies also indicated that prolonged immersion may densify the coating through the thickening of Al-hydroxide through the pores, gradually increasing impedance over time.[12–14,17,18]

Therefore, this study builds on the aforementioned findings[1,4,6,7] by investigating the role of conversion time in governing the long-term corrosion resistance of ZrCCs on AA5754, with particular focus on differences in polymerisation behaviour between IMPs and the surrounding matrix. Consequently, our main focus was not to prove ZrCCs' protection efficiency as standalone coatings, but rather to compare their performance in terms of conversion time and relate the results to the composition and morphology of the resulting coatings. Given the aforementioned predominantly cathodic nature of IMPs and their tendency to promote enhanced local ZrCC deposition, we hypothesise that distinct oligomers or polymeric species may preferentially form at these sites relative to the aluminium matrix.

*Electrochemical Society Member.
**Electrochemical Society Fellow.
[z]E-mail: ingrid.milosev@ijs.si; philippe.marcus@chimieparistech.psl.eu

Given the exceptional surface sensitivity of ToF-SIMS,[19] its ability to provide structural information from mass fragments, and its proven capacity to identify polymeric Zr species,[4,20–22] we aim here to extend its application to this context, where, to the best of our knowledge, it has not yet been employed.

Experimental

Materials and chemicals.—Aluminium alloy EN AW-5754 (denoted as AA5754) in the form of a 1.5 mm thick panel was supplied by Impol 2000 d.d., Slovenska Bistrica, Slovenia. The following chemical composition was specified by the manufacturer: Mg 2.6–3.6 wt%, Mn 0–0.5 wt%, Si 0–0.4 wt%, Fe 0–0.4 wt%, Cr 0–0.3 wt%, Zn 0–0.2 wt%, Ti 0–0.15 wt%, Cu 0–0.1 wt%, Al remainder. Original panels were cut into 2.5 cm × 3.5 cm specimens with 3 mm holes for immersion in H_2ZrF_6 baths.[7] Smaller pieces ($\leqslant$1 cm^2) were prepared for ToF-SIMS.

All solutions were prepared using analytical-grade reagents: absolute ethanol (EtOH, Merck KGaA, Darmstadt, Germany), NaCl (Fisher Scientific, Leicestershire, UK), $(NH_4)_2SO_4$ (Acros Organics Geel, Belgium), NH_4HCO_3 (Sigma-Aldrich, Steinheim, Germany), H_2ZrF_6 (50 wt% in water, Sigma- Aldrich, Saint Louis, USA).

Chemical pretreatments were performed using SurTec® products, namely SurTec® 089, SurTec® 132, and SurTec® 496—supplied by SurTec Adria d.o.o. (Ljubljana, Slovenia) and produced by SurTec International GmbH (Bensheim, Germany). SurTec® 089 is a concentrated detergent booster containing non-ionic surfactants based on ethoxylated fatty alcohols and amine derivatives, which enhance the removal of organic contaminants such as oils and processing residues. SurTec® 132 is a slightly alkaline builder, free of silicates and surfactants, primarily based on tetrapotassium pyrophosphate ($K_4P_2O_7$), which acts as a buffering and complexing agent for multivalent metal ions. SurTec® 141 is an alkaline builder without surfactants, containing phosphates, sodium tetraborate and silicates, which increase bath alkalinity and provide buffering and complexation during alkaline treatment of aluminium. SurTec® 496 is a concentrated acidic desmutting solution containing sulfuric acid, nitric acid, hydrofluoric acid and iron(III) salts, used to remove insoluble smut layers composed mainly of alloying-element-rich intermetallic particles and residual oxides, thereby producing a chemically clean surface suitable for subsequent conversion coating formation.

The solutions were prepared using Milli-Q Direct water from Millipore in Billerica, Massachusetts, USA, characterised by a resistivity $\geqslant$18.2 MΩ cm at 25 °C. Water with a total organic carbon (TOC) value below 5 ppb was employed for both rinsing samples and preparing solutions.

Mechanical pretreatment.—The initial step in sample preparation involved manual wet-grinding using SiC papers up to P4000 grit on a LaboPol-5 grinding/polishing machine operating at 300 rpm (rotation per minute) (Struers, Ballerup, Denmark). Following the grinding process, the samples were sonicated for 5 min in absolute ethanol using a 37 kHz, 100% power Elmasonic P ultrasonic bath for cleaning. Subsequently, the samples were rinsed with absolute ethanol and Milli-Q water before being dried using compressed N_2. Samples prepared by the grinding step are denoted as bare.

Chemical pretreatment.—Before the Zr conversion treatment, mechanically ground samples were chemically pretreated using alkaline cleaning and desmutting. The specimens were immersed in the respective SurTec® solutions on a C-MAG HS 7 magnetic hotplate stirrer (IKA®-Werke GmbH & Co. KG, Staufen, Germany). The stirring rate was set at 150 rpm, and the temperature was maintained at 60 °C, except for the desmutting step, which was conducted at room temperature (RT). The procedure following the laboratory-adapted recommendations provided by SurTec for aluminium alloys was used: a 10 min alkaline cleaning in 3 vol% (30 ml l^{-1}) SurTec® 132 + 0.5 vol% (5 ml l^{-1}) SurTec® 089, pH = 7.4, followed by a 3 min acid desmutting in 20 vol% (200 ml l^{-1}) SurTec® 496, pH = 0.3. Glass beakers with a volume of 500 mL were employed for rinsing step. Following each alkaline cleaning/desmutting step, a thorough double rinse with Milli-Q Direct water was conducted through two distinct steps: (i) an approximately 30 s vigorous circular rinse using a wash bottle on both sides of the sample, and (ii) a 1 min immersion in a clean Milli-Q Direct water bath. Samples prepared by the grinding step, followed by alkaline cleaning and desmutting, are denoted as alkaline cleaned and desmutted.

Conversion treatment.—Immediately after chemical pretreatment, the samples—still fully wet—were immersed in H_2ZrF_6 conversion baths at 150 ppm concentration for either 230 or 480 s (samples denoted ZrCC-230 and ZrCC-480). The conversion solutions were prepared by initially diluting a 50 wt% H_2ZrF_6 stock solution in a small volume of water. The solution was then brought to the final volume, with the pH adjusted to 4.6 under vigorous stirring using a diluted (15 wt%) NH_4HCO_3 solution. The pH was monitored using a pH meter 827 pH-lab connected to a Solitrode HF combined pH electrode suitable for measurements in HF and F-containing solutions (Metrohm AG, Herisau, Switzerland). The prepared H_2ZrF_6 solutions were stored in polyethylene bottles.

Conversion baths were set up in Teflon beakers (V = 250 ml). Samples were immersed in these baths and suspended from a plastic stick. Samples were gently moved back and forth through the conversion bath intermittently to allow fresh solution access to the surface, a practice occasionally observed in industrial settings with manual immersion. After the conversion process, the samples were rinsed in two stages: (i) a vigorous circular rinse on both sides using a wash bottle for approximately 30 s, and (ii) a 1 min dip in a clean Milli-Q Direct water bath. The samples were then dried with a stream of compressed N_2 from bottom to top, followed by an additional 10 min of drying on a C-MAG HP 4 hotplate (IKA®-Werke GmbH & Co. KG, Staufen, Germany) at 80 °C, following common industrial practices and left to air-dry for 24 h at room temperature (RT) due to the assessed beneficial the influence of drying on the results, as indicated in.[7]

Electrochemical impedance spectroscopy.—EIS measurements were performed using a three-electrode setup controlled by a Multi Autolab/M204 potentiostat/galvanostat (Metrohm Autolab, Utrecht, Netherlands) operated via NOVA 2.1 software. Experiments were conducted in custom-made "clamp-on" electrochemical cells (250 ml), specifically designed for flat, thin-coated samples to minimise the risk of crevice corrosion.[23]

The coated sample acted as the working electrode (WE), mounted at the bottom of the cell and sealed against an O-ring to allow gas bubbles generated during cathodic reactions to escape freely. A carbon rod served as the counter electrode (CE), while a saturated Ag/AgCl (3 M KCl) electrode (E = 0.297 V vs standard hydrogen electrode) was used as the reference electrode (RE), positioned close to the WE to minimise uncompensated iR drop. All reported potentials are referenced to the Ag/AgCl (3 M) scale. The exposed working electrode area was 0.785 cm^2. All measurements were conducted under ambient laboratory conditions.

Only samples dried for 24 h at RT were subjected to electrochemical testing, as the drying-induced growth of aluminium oxide improved their corrosion resistance.[7,12–14] Prior to electrochemical testing, samples were allowed to stabilise at open circuit potential (OCP) until a quasi-steady state was reached, typically within 1 h.[24] This stabilisation step was essential to avoid artefacts associated with surface alterations caused by excessive excitation during subsequent impedance measurements.

EIS measurements were then conducted at OCP using a ±10 mV RMS (root mean square) sinusoidal perturbation. Impedance spectra were recorded over a frequency range of 100 kHz to 10 mHz, with 51 logarithmically spaced frequency points across seven decades. Data

were analysed using NOVA 2.1 software and fitted to an equivalent electrical circuit model using the Levenberg–Marquardt optimisation algorithm. The measurement protocol and data interpretation followed the methodology described.[7] Dilute Harrison's solution (DHS, 3.5 g l^{-1} $(NH_4)_2SO_4$ and 0.5 g l^{-1} NaCl, pH = 5.2) was used as the electrolyte, providing sufficient aggressiveness to distinguish ZrCC performance without obscuring subtle differences in protection, as in our previous works.[4,7] DHS is a modification of the original Harrison's solution introduced by Timmins[25] and is designed to represent atmospheric corrosion environments. Compared with the commonly used 3.5 wt% NaCl solution, which simulates seawater conditions, DHS contains a much lower chloride concentration. The combination of sulfate and chloride ions better mimics the chemistry of thin electrolyte layers forming during atmospheric exposure, where sea-salt deposition and sulfate-containing pollutants may coexist. For this reason, DHS is widely used in Prohesion-type cyclic corrosion testing of organic coatings and primers[26–29] and has also been applied in electrochemical studies of coated systems.[30,31] The measurements showed good repeatability, and representative results from multiple runs are presented here. The measurements showed good repeatability, and representative results from multiple runs are presented here. The measurements showed good repeatability, and representative results from multiple runs are presented here.

Time-of-flight secondary ion mass spectrometry.—After conversion coating preparation and air-drying for 24 h, the samples were analysed by ToF-SIMS using a ToF-SIMS 5 instrument (IONTOF GmbH, Münster, Germany), operated at a base pressure of 5×10^{-9} mbar. Data acquisition and processing were performed using SurfaceLab software (version 7).

Mass spectra.—The instrument was operated in High Current (HC) bunched mode, achieving a high mass resolution ($\Delta M/M \approx 7000$, measured on the Si^- peak).

All measurements were conducted in negative ion mode. Calibration of the mass spectra was performed using the exact mass values of at least five well-identified negative ion species. Spectra were recorded over a mass-to-charge (m/z) range of 0–590, using a pulsed 25 keV Bi^+ primary ion beam (target current: 1.2 pA) rastered over a 500 μm × 500 μm area at a 45° incidence angle. To ensure static SIMS conditions, the primary ion dose was kept below 10^{12} ions·cm^{-2}.

Depth profiling and region-of-interest analysis.—Depth profiling was carried out in the Burst Alignement (BA) imaging mode by alternating between the analytical cycles using the Bi^+ ion beam (0.3 pA, 100 μm × 100 μm) with sputtering cycle using a 2 keV Cs^+ ion beam (100 nA) over a 500 μm × 500 μm area. The BA mode (8 peaks burst) provides high lateral resolution (around 150 nm) together with sufficient mass resolution ($\Delta M/M \approx 2000$, measured on the Si^- peak) to unambiguously distinguish the ions of interest. These operating conditions enable full 3D chemical characterization of the surface and near surface region.

Both ion beams were incident at 45° relative to the sample surface, with alignment optimised to ensure profiling at the centre of the sputtered crater. The intensities of selected ion fragments were recorded quasi-simultaneously and plotted as a function of Cs^+ sputtering time. To confirm reproducibility, depth profiles were collected from two distinct regions on each sample surface.

In addition to global depth profiles (averaged across the complete analysis area), region-of-interest (ROI) analyses were performed to distinguish between intermetallic particles and matrix regions. ROIs were defined on corresponding ion images, enabling direct comparison of speciation and coating behaviour at different microstructural sites.

Atomic force microscopy and contact angle measurements.—Atomic force microscopy (AFM) imaging was performed using a Park NX20 system (Park Systems) operated with SmartScan™ software. A high-frequency ACTA cantilever with a backside reflective coating (Park Systems) was employed. The cantilever had a pyramidal tip with a radius of 6 nm and a length of 14–16 μm, operating at a resonance frequency of 300 kHz. Scans were acquired in non-contact mode over a 10 μm × 10 μm area at a scan rate of 0.3 Hz. Surface roughness was evaluated from the AFM data across the entire surface to obtain the arithmetical mean height, S_a, as well as separately for the aluminium matrix and IMPs.

Surface wettability was assessed by static contact angle measurements using an Ossila goniometer (Ossila Ltd.) equipped with a high-resolution 1920 × 1080 camera. The instrument allowed measurement of apparent contact angles of a water drop between 5° and 180° with an accuracy of ±1°. Contact angles, θ, were determined after two drying regimes[7]: 10 min at 80 °C and 24 h at RT, enabling evaluation of the time-dependent evolution of surface wettability.

Results and Discussion

Corrosion resistance of ZrCCs investigated by EIS.—The conditions for ZrCC deposition (150 ppm, pH 4.6 at either 230 and 480 s) were selected based on previously identified[7] optimal behaviour in EIS and SEM/EDS analyses, which resulted in the highest polarisation resistance (R_p) values and the least cracking around IMPs.

The recorded EIS spectra (Nyquist plots in Fig. 1, Table S1) were fitted with a simple Randles circuit ([R1(R2CPE1)], inset in Fig. 1), as described by Buchheit et al.[32] R1 represents electrolyte resistance, R2 the resistance of exposure-induced defects, and CPE1 the interfacial capacitance. Pore impedance and charge transfer contributions are likely incorporated into $R_p = R2 + R3 + \cdots + Rn$. A constant phase element (CPE) was used instead of a capacitor to account for relaxation time dispersion from surface inhomogeneities.[33] Please note that data for the non-ZrCC-treated sample results have been taken from Ref. 7 for comparison purposes only.

The inductive behaviour observed at low frequencies showed no discernible pattern and was not related to pitting, as confirmed by visual inspection (not shown). Instead, this behaviour is more likely attributable to surface roughness, adsorption phenomena, or ion exchange processes,[10,34] potentially involving Cl^- and F^-, as indicated by the X-ray photoelectron spectroscopy (XPS) study of Šekularac et al.[14]

Overall, the capacitive arcs of ZrCC-coated specimens are significantly smaller than those of uncoated, alkaline-cleaned, and desmutted substrates, indicating that ZrCCs do not enhance short-term corrosion protection, consistent with previous work.[7] This behaviour is attributed to cracks forming at IMP sites, which allow electrolyte penetration and create corrosion pathways. Prolonged conversion time had little influence on coating behaviour, as evidenced by the similar R_p values obtained (Table SI). It is important to note that ZrCCs are inherently very thin, typically 10–80 nm,[35] regardless of processing conditions, and unlike traditional chromate conversion coatings, they do not possess self-healing capability.[36] Consequently, their primary function in practical applications is not to provide standalone corrosion protection but rather to promote adhesion within multilayer coating systems, especially in automotive and aerospace applications.[35] For this reason, substantial improvements in standalone corrosion resistance are generally not expected, and the objective is instead to identify processing conditions that provide comparatively better performance within the intrinsic limitations of such thin coatings.

To build on our previous RSM study,[7] the conditions of 150 ppm, 230 s, and pH 4.6 were selected because they yielded the most favourable coating performance, as indicated by EIS and SEM results. Conditions outside the optimal processing window generally resulted in lower R_p values, most likely due to excessive coating cracking, and were therefore not investigated further. Nevertheless, the measured R_p values across the investigated parameter space

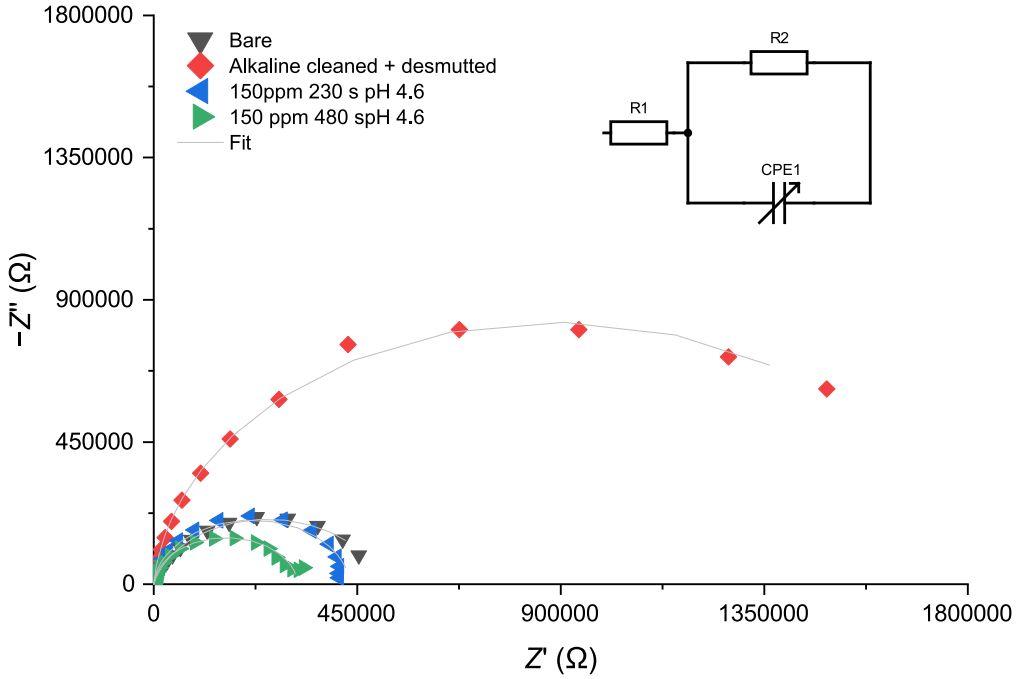

Figure 1. EIS Nyquist plots of bare (ground), pretreated (alkaline-etched and desmutted), and ZrCC-coated AA5754 samples are shown. The ZrCCs were formed from a 150 ppm H_2ZrF_6 conversion bath (pH 4.6) with conversion times of 230 s and 480 s. EIS measurements were performed in dilute Harrison's solution after 1 h of immersion. The inset shows the equivalent electrical circuit (EEC) used for fitting.

remained within the same order of magnitude, highlighting the importance of statistical analysis to identify meaningful differences. Based on previous studies and literature findings, the optimal conditions identified here are likely applicable to most aluminium alloy series due to similarities in the reactivity of cathodic IMPs.[13,37–39] An exception may be the 2xxx series alloys, where highly cathodic Cu-rich intermetallic particles significantly accelerate the conversion reaction. In such cases, shorter conversion times or higher bath pH values may be required to reduce coating cracking.

Within the RSM design space, the ZrCC-480 showed slightly higher predicted R_p values than ZrCC-230; however, both 230 s and 480 s represent high-leverage points ($h \approx 0.41$ and $h \approx 0.76$, respectively) located at the edge of the parameter space. This means that small experimental variations can strongly affect model predictions.

Despite deviations between the measured and predicted R_p values —particularly for the 480 s condition—all results remain statistically within the model's tolerance intervals. These intervals define the expected range of experimental outcomes (99% of the population with 95% confidence). Practically, this indicates that although the ZrCC-480 exhibits somewhat lower resistance, the observed experimental variation is not unexpected and remains consistent with the statistical uncertainty inherent to the model. A more detailed explanation is given in the Supplementary material.

Composition and structure of the ZrCC analysed by ToF-SIMS

High-resolution mass spectra (Fig. S1) recorded at the surface of ZrCC-230 and ZrCC-480 samples in the m/z range 0–590 revealed peaks corresponding to monomeric species (120–160 m/z), dimeric (240–290 m/z), and trimeric (380–420 m/z) zirconium species, with tetrameric fragments (500–540 m/z) detected only at very low intensities. Assignments are listed in Table SII. Note that the table also includes $Zr_nO_m(OH)_pF_q^-$ fragments, consistent with fluoride incorporation as oxyfluorides,[15,40] likely via isomorphic substitution of F^- for OH^- during ZrF_6^{2-} hydrolysis.[1] Since ToF-SIMS cannot distinguish oxide- from hydroxide-derived oxygen, fragments were reported as $Zr_nO_mH_p^-$ and $Zr_nO_mH_pF_q^-$, though $Zr_nO_m(OH)_p^-$ would be chemically more precise. Monomeric species ZrO_2^-, $ZrO_3H_3^-$ show high intensity in the region 120–160 m/z, whereas $ZrO_2H_3^-$ species are somewhat less (Fig. S1). However, the spectra in the higher m/z regions corroborate the presence of dimeric ($Zr_2O_5H_3^-$), trimeric ($Zr_3O_7H_7^-$) and tetrameric ($Zr_4O_9H_8^-$) species as well. These results confirm our previous experimental data on CRS and imply that a similar deposition mechanism, including thermodynamically predicted polymerised Zr −OH forms, is also operative for Al alloy. Among polymeric species, the tetrameric ones show the lowest intensity.

Negative ion depth profiles (Fig. 2), commonly employed to investigate oxide species,[41–44] were plotted on a logarithmic scale to emphasise low-intensity signals. Global depth profiles were first obtained over the complete analysis area, followed by region-of-interest (ROI) analyses. The latter were extracted separately from the intermetallic particle (blue) and matrix (green) zones (Figs. 3d, 3j, 3f, 3l), with profiles normalised according to their respective surface areas. For the ZrCC-230, IMPs accounted for 2.7%, and the matrix for 18.1% of the analysed surface; for the ZrCC-480, the corresponding values were 4.8% and 9.8%. Depth profile intensities for ROIs in Figs. 2b, 2c, 2e, 2f were normalised to these areas. Intensity variations reflect compositional changes with depth, but are strongly affected by the emission matrix[45] and surface roughness,[46] so the profiles can be interpreted comparatively rather than quantitatively.

When making depth profiles, the most representative and intense signals from Fig. S1 and Table SII were used. Three depth regions were consistently distinguished in global profiles (Figs. 2a, 2d). The outer ZrCC layer was characterised by a highest plateau of ZrO_2^- and an inner layer of a highest plateau of AlO_2^- signals. The bilayer structure is denoted by the intersection of the ZrO_2^- and AlO_2^- signals at the vertical grey line. Following the intersection, the ZrO_2^- signal declined and the concurrent rise of AlO_2^- and, especially, Al_2^- occurred. The intersection of AlO_2^- and Al_2^- signals is represented by the vertical red line denoting the ZrCC/substrate interface. The region of metallic substrate was recognised by a plateau in Al_2^- intensity.

Comparing the shape of the profiles for ZrO_2^- and AlO_2^-, it is evident that the extent of the plateaus formed is broader for the ZrCC-480 than for ZrCC-280. Assuming a nominal sputtering rate of 0.18 nm·s^{-1} (as reported for TCP coatings[19]), the crossover ZrO_2^-/AlO_2^- occurred after ∼50 s for the ZrCC-230 (∼9 nm) and ∼120 s for the ZrCC-480 (∼21 nm), confirming that the thickness of the outer ZrCC layer increased with conversion time (Table I).

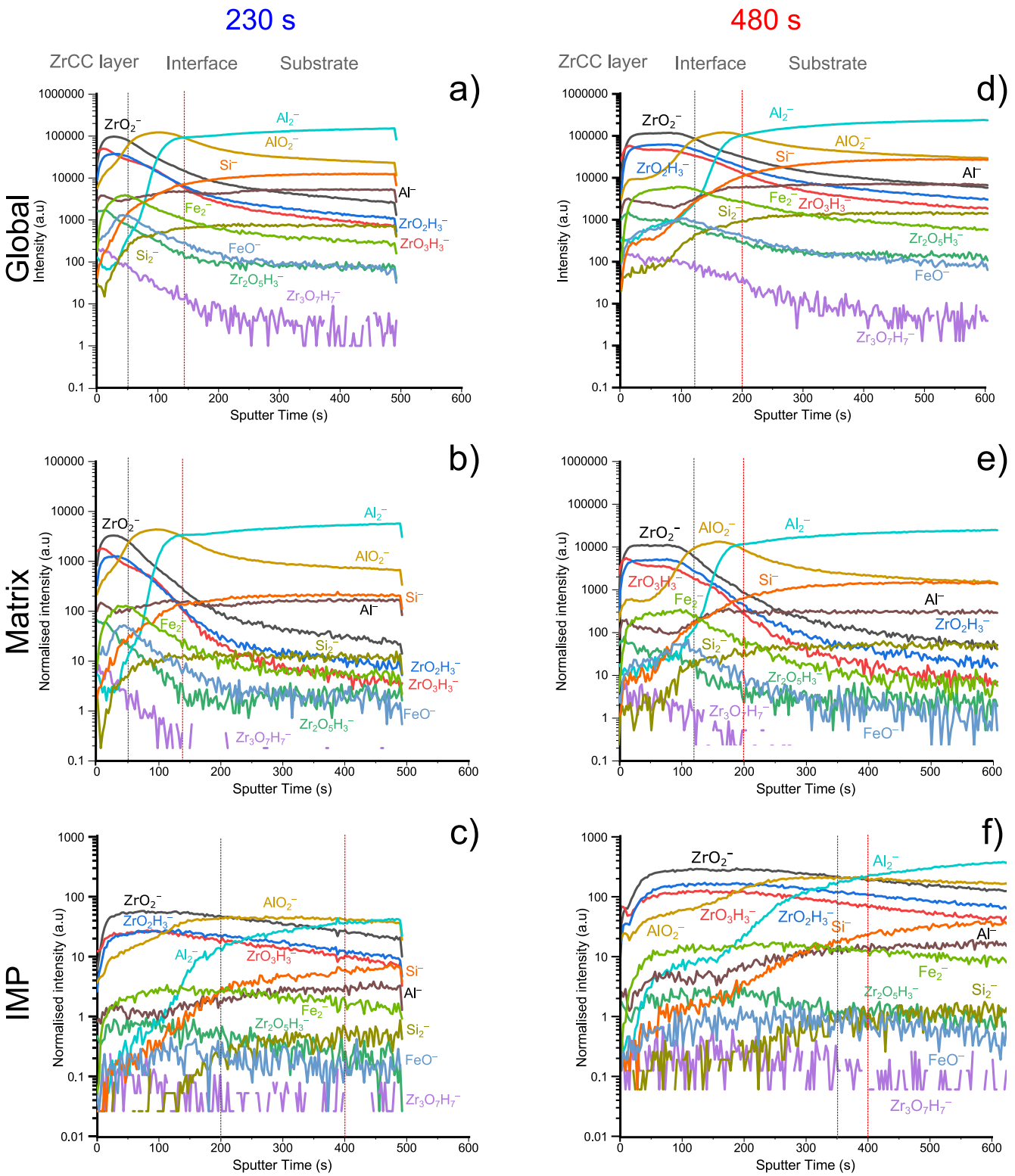

Figure 2. ToF-SIMS negative ion depth profiles of AA5754 coated with ZrCCs prepared at 150 ppm H_2ZrF_6, pH 4.6, for 230 s (a)–(c) and 480 s (d)–(f) conversion times: (a), (d) global, (b), (e) matrix, and (c), (f) intermetallic particle (IMP) profiles.

In both cases, the gradual rise of Al_2^- was consistent with interfacial roughness[47] and the contribution of the native oxide, which appears unaffected by conversion time. For ZrCC-230 and ZrCC-480, the Al_2^- signal reached a pseudo-maximum intensity at around 140 and 200 s of sputtering, respectively. At the same time, the progressive decline in AlO_2^- signal occurred. The depth profiles confirm that the Zr-based layer is enriched at the outer part of the coating, whereas the Al oxide is at the inner interface. Let us first calculate the total ZrCC thickness corresponding to the sputter time at the intersection AlO_2^-/Al_2^- (vertical red line), denoting the interface between the ZrCC and the metal substrate (Table I). For the ZrCC-230, the line is at 140 s, and for the ZrCC-480 is at 200 s; translated to thickness, these values amount to 25 nm and 36 nm, respectively. The thickness of the inner part of the ZrCC is now

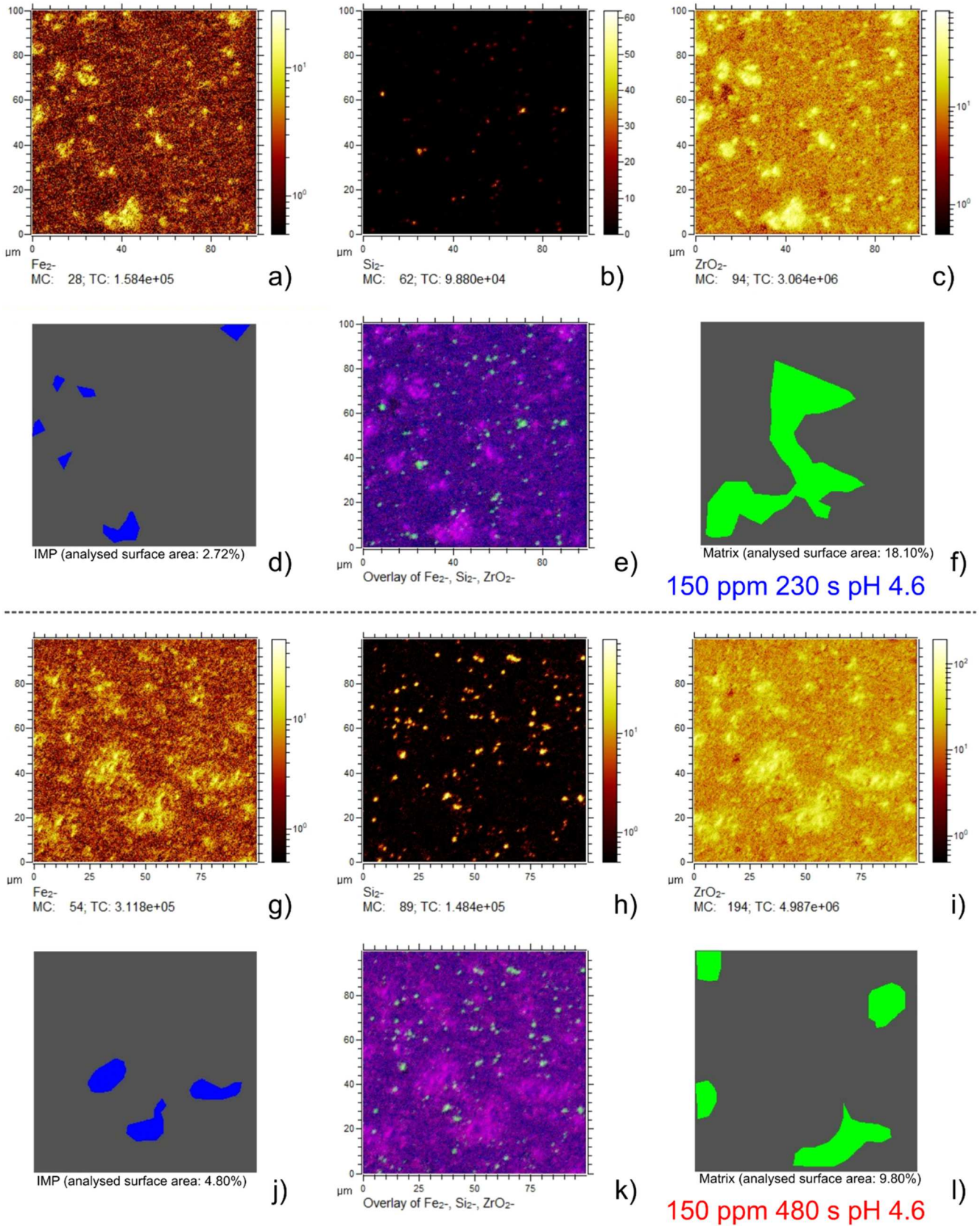

Figure 3. ToF-SIMS negative ion images of AA5754 coated with zirconium conversion coatings (ZrCCs), prepared using 150 ppm H_2ZrF_6 at pH 4.6, for conversion times of 230 s (a–f) and 480 s (g–l). The distributions of Fe_2^- (a), (g), Si_2^- (b), (h), and ZrO_2^- (c), (i) ions are shown, along with their overlays (e), (k). Regions of interest are indicated for intermetallic particles (IMPs, blue; (d), (j)) and for the matrix (green; (f), (l)).

Table I. The thickness of the outer and inner layers of the ZrCC derived from ToF-SIMS profiles in Fig. 2.

	Thickness/nm (sputtering time at the intersection/s)					
	Conversion time 230 s			Conversion time 480 s		
Site	Outer layer	Inner layer	Total	Outer layer	Inner layer	Total
global/matrix	9 nm (50 s)	16 nm (90 s)	25 nm (140 s)	21 nm (120 s)	15 nm (80 s)	36 nm (200 s)
IMP	36 nm (200 s)	36 nm (200 s)	72 nm (400 s)	63 m (350 s)	>90 nm (>500 s)	

calculated as the difference between the total thickness and the thickness of the outer part of the ZrCC, denoted by the area between two vertical lines. For the ZrCC-230, it amounts to 16 nm, and for the 480s-treatment, 15 nm. It seems that prolonging the conversion time from 230 s to 480 s primarily affects the outer Zr-based layer, increasing its thickness from 9 to 21 nm, rather than that of the inner layer. Namely, in both cases, the latter thickness was ∼15–16 nm.

ROI-specific analyses of the matrix (Figs. 2b, 2e) and IMP (Figs. 2c, 2f) revealed pronounced local differences compared to the global analysis. Whereas matrix profiles largely mirrored the global response, IMP profiles exhibited prolonged ZrO_2^- signals and delayed Al_2^- onset, indicative of locally thicker coatings. For the ZrCC-230 (Fig. 2c), the crossover occurred at ∼200 s (∼36 nm), with the substrate detected only after ∼400 s (∼72 nm) (Table I). For the ZrCC-480 (Fig. 2f), the ZrO_2^- signal persisted until ∼350 s of sputtering (∼63 nm), with substrate onset after ∼400 s (∼72 nm). Al_2^- continued to rise beyond the sputtering time of 500 s, reflecting interface complexity and roughness and inability to distinguish thicknesses of the inner layer correctly. Over IMPs, transitions were less distinct than at the matrix. These data confirm that the ZrCC thickness is distinctly larger at the IMPs than at the matrix. The extended conversion time primarily increases the thickness of the outer coating layer.

Element-specific signals provided additional information. Although Fe_2^- intensities were much weaker than ZrO_2^-, their depth profiles exhibited a similar trend, peaking near the ZrCC/substrate interface and declining with sputtering depth. In the matrix (Figs. 2b, 2e), the sharp decrease in Fe concentration below the interface suggests that these particles are confined to the interface region, with little to no Fe enrichment in the underlying substrate. For IMPs (Figs 2c, 2f), Fe_2^- signal remained at the same level, also below the interface, confirming that the preferential growth of ZrCC is related to the presence of cathodic sites, in this case, Fe-rich IMPs, Si^- signals were weak, in line with the low Si content in AA5754.

Let us look more closely at the distribution of polymerised Zr forms (Figs. 2 and S2, where only Zr-related fragments are shown). Although detected at the surface (Fig. S1), the signal of the tetrameric species was not included in the depth profiles due to its low intensity. At the surface, monomeric ZrO_2^- species prevailed, followed by other monomeric forms of $ZrO_3H_3^-$ and $ZrO_2H_3^-$. Dimeric $Zr_2O_2H_5^-$ species were of lesser intensity than monomeric ZrO_2^- but close to that of $ZrO_2H_3^-$. Trimeric $Zr_3O_7H_7^-$ species exhibited the lowest intensity. From the surface to the layer depth, the intensity of monomeric Zr species increased to a maximum before declining toward the inner interface. In contrast, the intensities of the dimeric and trimeric species decreased rapidly within the layer. This feature may indicate that the polymerised species are predominantly present at the surface rather than in the layer bulk; however, since sputtering may induce at least partial fragmentation[48,49] of these oligomers[a], this assumption cannot be directly proven. However, it seems logical to assume that the fragmentation of oligomer species to monomers would increase the intensity of the latter species with the layer bulk, as observed experimentally.

It is well established that the degree of Zr polymerisation increases with both pH and [Zr], being strongly dependent on initial conditions—Zr concentration, solution ageing, pH, and the presence of complexing ligands.[2,3,50–53] In particular, combined X-ray Absorption Fine Structure (XAFS) and Electrospray Ionization Mass Spectrometry (ESI-MS) studies of fluoride-free Zr solutions ([Zr] = 1.5–10 mM, pH_c 0–3, where pH_c is pH_c = concentration pH, differing from activity pH by a constant at fixed ionic strength[54]) have shown a continuous hydrolysis–condensation sequence in which coordinated H_2O ligands are progressively replaced by OH^-, yielding charge-compensated polynuclear species ranging from monomers to dodecamers.[50] In particular, at low millimolar Zr concentrations, pertaining to the concentration range of interest for ZrCCs,[35] it has been reported that hydrolysed Zr(IV) is dominated by the cyclic tetramer $[Zr_4(OH)_8(H_2O)_{16}]^{8+}$, accompanied by small fractions of dimers and other low-order oligomers.[50,55] With increasing concentration, this tetrameric core remains the principal structural unit but progressively coexists with larger μ-OH/μ-O-bridged oligomers and early-stage Zr–O–Zr network formation, a trend consistently observed in solution studies extending into the several-millimolar regime.[56–58]

Although trimers have been observed at increased acidities (>1 M), their stability remains debated, with recent Car–Parrinello molecular dynamics simulations suggesting that the trimer is likely a transient intermediate en route to tetramer formation.[59] For context, the incorporation of tetrameric units, represented as $Zr_4(OH)_8^{8+}$, was long ago proposed by Clearfield for amorphous zirconia.[5] Its persistence is attributed to cyclisation-stabilised kinetics, which facilitate its incorporation from aqueous precursors into the solid oxide. Assuming a general relationship between species in the solution and those forming the solid phase[3]—and considering that fluoride ions from H_2ZrF_6 are exchanged with OH^- during the alkalisation accompanying ZrCC deposition—it is plausible that tetrameric units participate in the formation of amorphous ZrCCs. This was supported by our previous ToF-SIMS study on cold-rolled steel,[4] in which tetrameric zirconium species ($Zr_4O_7H_7^-$) were clearly detected at pH ≈ 4, corresponding to the conditions under which ZrCC films were actively forming. In H_2ZrF_6-containing baths, fluoride perturbs the primary ligand environment yet does not alter the fundamental polymerisation topology. The solutions are therefore expected to contain fluoro–hydroxo analogues of the same tetrameric and higher oligomeric Zr–O species, with the degree of polymerisation increasing systematically with both pH and total zirconium concentration.

In contrast, the present ToF-SIMS investigation on aluminium alloy (AA5754) at pH 4.6 revealed predominantly trimeric zirconium species, with tetrameric fragments ($Zr_4O_9H_8^-$, $Zr_4O_{10}H_9^-$/$Zr_4O_9H_6F^-$) appearing only at very low, insignificant intensities (Fig. S1). The absence of significant tetrameric signals on aluminium suggests that distinct condensation and deposition pathways operate on different substrates. Given the fragmentary nature of ToF-SIMS, both trimeric and tetrameric species are best interpreted as fragments of larger, condensed polynuclear entities rather than discrete clusters; nevertheless, their consistent presence or absence offers meaningful mechanistic insight.

[a]According to the IUPAC guide to polymer terminology,[48] a polymer is a substance composed of macromolecules in which a large number of structural units (monomers) are covalently bonded in a chain-like or network structure. When only a few monomer units are linked together, the resulting molecule is referred to as an oligomer, representing a lower molecular-weight counterpart of a polymer. Thus, oligomers consist of a small plurality of repeating units, while polymers contain a large number of such units, often forming extended chains or three-dimensional networks.[49]

Table II. AFM surface roughness results, S_a for AA5754 samples with different ZrCC treatments, including analysis on both IMP and the matrix. AFM images are presented in Fig. S3.

Sample	S_a/nm	S_a IMP/nm	S_a matrix/nm
Bare (polished), 24 h at RT	22	—	—
Alkaline cleaned+desmutted, 24 h at RT	127	212	56
H_2ZrF_6 150 ppm/230 s/pH 4.6, 24 h at RT	87	360	52
H_2ZrF_6 150 ppm/480 s/pH 4.6, 24 h at RT	68	259	32

Table III. Contact angle results for AA5754 samples with different ZrCC treatments. Protective ability (PA) values were taken from Ref. 7 for comparison purposes.

Sample	Contact angle, θ/°	Average PA/s
Bare, 10 min at 80 °C	28 ± 6	11
Bare, 24 h at RT	69 ± 2	12
Alkaline cleaned, 10 min at 80 °C	∼0	28
Alkaline cleaned, 24 h at RT	19 ± 2	36
Alkaline cleaned+desmutted, 10 min at 80 °C	∼0	35
Alkaline cleaned+desmutted, 24 h at RT	48 ± 5	52
H_2ZrF_6 150 ppm/230 s/pH 4.6, 10 min at 80 °C	∼0	20
H_2ZrF_6 150 ppm/230 s/pH 4.6, 24 h at RT	29 ± 2	80
H_2ZrF_6 150 ppm/480 s/pH 4.6, 10 min at 80 °C	∼0	14
H_2ZrF_6 150 ppm/480 s/pH 4.6, 24 h at RT	41 ± 6	51

Although sputtering-induced fragmentation may underrepresent higher-order species, the consistent detection of tetramers on CRS indicates that their absence on aluminium is not merely an analytical artefact but reflects fundamental differences in the deposition mechanism. This also raises the question of whether tetrameric polymeric forms are required to establish a protective ZrCC coating, as hypothesised for steel.[4]

Furthermore, the detection of predominantly lower-order species on aluminium suggests a smaller local pH increase during deposition. This hypothesis will be verified in our future work,[60] since the higher cathodic activity of IMPs relative to the surrounding matrix results in a different pH evolution in those regions. However, the overall effect is likely to be a weaker alkalisation, which may in turn limit the extent of Zr polymerisation.

Finally, ToF-SIMS mapping (Fig. 3) corroborated the depth profile results, with IMP corresponding to Fe enrichment (Figs. 3a, 3g), while the surrounding matrix shows the opposite composition. The ZrO_2^- signal intensities were lower for the ZrCC-230 (Figs. 3c) than for the ZrCC-480 (Fig. 3i), while substrate-related signals (Fe_2^-, compare Figs. 3a, 3g and Si_2^- compare Figs. 3b, 3h) were higher. This is consistent with the thinner nature of the former and with the higher ZrCC deposition on IMPs, in agreement with SEM/EDS data from our previous study.[7]

Roughness and wettability data analysed by AFM and contact angle data.—Table II presents the surface roughness expressed as S_a, derived from AFM images in Fig. S3. S_a was evaluated across the entire imaged surface, while S_a IMP and S_a matrix were assessed separately by line-scan analysis across selected IMPs and adjacent matrix regions. The IMPs selected for AFM line-scan analysis were chosen to be representative of the coarse, surface-visible constituent particle population typically present in wrought AA5754[b]. Previous microstructural studies of AA5754 have shown that the μm-scale constituent particle population is dominated by Fe/Mn-bearing intermetallic phases, primarily (Mn,Fe)Al_6, with a smaller contribution from α-Al(Fe,Mn)Si-type particles; when particles larger than ∼1–3 μm are considered, these Fe/Mn-rich phases constitute the great majority of coarse IMPs and exhibit characteristic sizes on the order of a few micrometres.[61–63] This limited phase diversity at the micrometre scale implies that AFM-derived roughness values are governed mainly by particle size and surface morphology rather than by variations in IMP chemistry.

Table III contains water contact angle (θ) results obtained from contact angle images in Fig. S4. For comparative purposes of the effect of chemical pretreatment on the corrosion performance of the non-coated and ZrCC-coated samples, the results for the protective ability[c] (PA) are presented.[7,64] A more detailed description is given in our previous study.[7]

The bare aluminium surface exhibited relatively low roughness (S_a = 22 nm after 24 h) and moderate wettability ($\theta = 69 \pm 2°$), but poor PA (12 s). Alkaline cleaning increased hydrophilicity immediately after treatment ($\theta \approx 0°$ after 10 min) and improved PA (28 s). After 24 h, however, the surface became more hydrophobic ($\theta = 19 \pm 2°$) while PA improved slightly (36 s).

When combined with desmutting, alkaline cleaning produced a surface that remained completely wettable at 10 min at 80 °C and exhibited higher PA (35 s). After 24 h, θ increased to 48 ± 5°, indicating a shift towards hydrophobicity, accompanied by higher PA (52 s). AFM confirmed that this pretreatment significantly increased roughness (S_a = 127 nm), particularly at IMPs (212 nm vs 56 nm on the matrix), consistent with selective dissolution and enhanced surface activation.

Deposition of ZrCCs further modified the surface morphology and wettability. The 230s-treatment produced an initially fully wettable surface ($\theta \approx 0°$) with low PA (20 s), which after 24 h

[b]The AFM analysis was not intended to provide a statistical quantification of the surface area fraction covered by IMPs, nor to be directly comparable to particle populations analysed by ToF-SIMS herein. Owing to the fundamentally different sampling areas and spatial scales of the two techniques—AFM probing individual surface features over micrometre-scale regions, and ToF-SIMS averaging chemically specific information over much larger surface areas through ROI analysis—a direct comparison of IMP size distributions or surface coverage between AFM and ToF-SIMS is not meaningful. Instead, the two techniques provide complementary information, with AFM offering local morphological context and ToF-SIMS capturing statistically averaged chemical behaviour and depth-resolved trends over larger analysed areas.

[c]PA values were obtained using a direct, non-electrochemical method known as the drop test. This method involves measuring the time, in seconds, required for the coating to completely dissolve. The dissolution is indicated by a colour change, signifying that the reduced reagent cations have reached the bare metal surface. For AA5754, "Akimov's reagent" [64] was used (82 g L^{-1} $CuSO_4 \cdot 5H_2O$, 33 g L^{-1} NaCl, and 13 mL L^{-1} of 0.1 N HCl, pH = 3.6). The time required for the colour change was measured with a stopwatch. The response obtained from this test is hence referred to as the "protective ability" (PA); a longer time for colour change indicates a higher PA).

evolved to moderate hydrophilicity ($\theta = 29 \pm 2°$) and substantially improved PA (80 s). AFM revealed high roughness ($S_a = 87$ nm), driven by pronounced growth at IMPs (360 nm vs 52 nm in the matrix).

The ZrCC-480 followed a similar trend but with distinct differences. Immediately after deposition, the surface was fully wettable ($\theta \approx 0°$) yet with poor PA (14 s). After 24 h, the contact angle increased to $41 \pm 6°$, and PA increased to 51 s. AFM showed lower roughness compared to the 230 s treatment ($S_a = 68$ nm), with preferential thickening at intermetallic sites (259 nm vs 32 nm in the matrix).

It should be noted that, since all samples were exposed to ambient air after processing, a thin layer of adventitious carbon inevitably formed.[65–68] However, because all surfaces experienced identical exposure conditions (after 10 min or 24 h), this contamination occurred uniformly under the given conditions and, in our view, does not affect the validity of the relative comparisons. More importantly, in addition to carbon uptake, natural ageing of aluminium-based surfaces during the first 24 h in air leads to slight oxide thickening and structural rearrangement. The presented results confirm that chemical pretreatments and ZrCCs initially increase surface hydrophilicity by generating hydroxyl-rich sites, thereby promoting the adhesion of subsequent organic topcoats, such as epoxy layers, as previously shown.[69,70] However, drying in air progressively reduces hydrophilicity while increasing protective ability.[71–73] This evolution is most pronounced for the 230s-treatment, which transitioned from complete wetting ($\theta \approx 0°$) and low PA (20 s) immediately after deposition to moderate hydrophilicity ($\theta = 29 \pm 2°$) and high PA (80 s) after 24 h. The ZrCC-480 exhibited the same trend, but with lower final protective performance ($\theta = 41 \pm 6°$; PA = 51 s).

Conclusions

The present study aimed to investigate, using ToF-SIMS, whether polymeric, in particular tetrameric, species are formed during the deposition of a zirconium conversion coating on aluminium alloy 5754. While the concentration of the conversion bath and pH were kept constant, ZrCC were prepared at two conversion times, 230 s and 480 s. ToF-SIMS confirmed that the monomeric ZrO_2^-, $ZrO_3H_3^-$ and $ZrO_2H_3^-$ were the most prevailing Zr species at the surface, followed by dimeric ($Zr_2O_5H_3^-$) and trimeric ($Zr_3O_3H_7^-$). This distribution is valid for the matrix and intermetallic particles. Moving from the substrate to the layer depth, the intensity of monomeric species increased, possibly due to oligomer fragmentation. The thickness of the ZrCC layer increases with conversion time, from ~25 nm to ~36 nm at the matrix, and from 72 nm to >90 nm at the IMPs. In both cases, the Al-hydroxide layer forms at the coating/substrate interface. ZrCC formation preferentially initiates at Fe-containing IMPs.

The identification of Zr-hydroxide polymeric species in ZrCC deposited on AA5754 confirms the thermodynamic predictions and previously experimentally obtained results on cold-rolled steel. However, while the tetrameric zirconium form in ZrCCs has been confirmed on cold-rolled steel using ToF-SIMS, further investigation on the aluminium alloy AA5754 using ToF-SIMS revealed polymeric species only up to trimers on both IMPs and the matrix. This observation correlates with a lower overall pH increase during ZrCC formation on IMPs and an aluminium matrix. These findings highlight how both substrate type and solution chemistry critically influence ZrCC speciation, leaving the exact structure of the solid ZrCC film an open question.

Electrochemical impedance spectroscopy after one hour of immersion showed that prolonged conversion time from 230 s to 480 s had little effect on overall corrosion behaviour. ZrCC-coated AA5754 samples, in fact, performed slightly worse than bare and desmutted substrates, owing to cracking initiated at IMPs. Nyquist plots consistently revealed a single time constant, with smaller capacitive arcs for ZrCC-coated samples, indicating that ZrCCs do not provide superior corrosion protection under the studied conditions.

AFM analysis confirmed preferential deposition and greater coating thickness at IMPs relative to the matrix, driven by local cathodic activity. Shorter conversion times (230 s) produced rougher but more protective coatings than longer times (480 s), suggesting that over-deposition yields thicker yet less compact films prone to cracking. Contact angle and protective ability measurements (as shown in our previous publication[7]) further demonstrated that ZrCCs evolve with time, transitioning from highly hydrophilic immediately after deposition to moderately hydrophobic after 24 h, with corresponding improvements in short-term protective behaviour.

Overall, these results indicate that the protective performance of ZrCCs on AA5754 is controlled not by roughness or wettability alone, but by coating compactness and uniformity. Unlike chromate conversion coatings, which suppress cathodic activity at IMPs and promote matrix growth, ZrCCs continue to accumulate preferentially at IMPs without self-limiting behaviour. This leads to stress accumulation and cracking, underscoring the need for future studies on local pH changes during conversion on aluminium alloys, as well as on the effect of prolonged exposure to corrosive environments and increasing coating thickness. Future studies will address the impact of longer immersion times in corrosive solutions, aiming to determine whether thicker ZrCC layers formed over extended conversion times improve the EIS response.

Acknowledgments

The authors gratefully acknowledge Dr Denis Sačer (Department of Physical and Organic Chemistry, Jožef Stefan Institute) for AFM data acquisition and Dr Chenyang Xie (Department of Physical and Organic Chemistry, Jožef Stefan Institute) for assistance with plotting high-resolution mass spectrometry data.

Funding

The authors acknowledge the financial support from the Slovenian Research and Innovation Agency (ARIS) through research core funding grant P2–0393 and project PR-09806, as well as the funding of the collaboration between Slovenia and France through the Proteus project "Integrated approach to the understanding of mechanisms of corrosion and protection of metals," financed by the ARIS and Campus France, respectively, in the period 2024–2025. The partial funding of the ToF-SIMS equipment by Région Île-de-France is also gratefully appreciated.

ORCID

Ana Kraš https://orcid.org/0000-0002-3499-0853
Ingrid Milošev https://orcid.org/0000-0002-7633-9954
Antoine Seyeux https://orcid.org/0000-0002-3062-8961
Philippe Marcus https://orcid.org/0000-0002-9140-0047

References

1. A. Kraš and I. Milošev, *J. Electrochem. Soc.*, **170**, 21508 (2023).
2. R. E. Connick and W. H. McVey, *J. Am. Chem. Soc.*, **71**, 3182 (1949).
3. T. E. Macdermott, *Coord. Chem. Rev.*, **11**, 1 (1973).
4. A. Kraš, I. Milošev, A. Seyeux, and P. Marcus, *Npj Mater. Degrad.*, **8**, 65 (2024).
5. A. Clearfield, *Rev. Pure Appl. Chem.*, **14**, 91 (1964).
6. A. Kraš, D. Kramar, and I. Milošev, *Corros. Sci.*, **242**, 112551 (2024).
7. A. Kraš, D. Kramar, and I. Milošev, *Corros. Sci.*, **249**, 112824 (2025).
8. P. Campestrini, H. Terryn, J. Vereecken, and J. H. W. de Wit, *J. Electrochem. Soc.*, **151**, B359 (2004).
9. P. Campestrini, E. P. M. van Westing, and J. H. W. de Wit, *Electrochim. Acta*, **46**, 2553 (2001).
10. D. Peng, J. Wu, X. Yan, X. Du, Y. Yan, and X. Li, *J. Coat. Technol. Res.*, **13**, 837 (2016).
11. B. S. Tanem, O. Lunder, and O. Ø. Knudsen, *Local Probe Techniques for Corrosion Research* (Elsevier, Amsterdam)99 (2007).
12. G. Šekularac and I. Milošev, *J. Electrochem. Soc.*, **167**, 021509 (2020).
13. G. Šekularac, J. Kovač, and I. Milošev, *J. Electrochem. Soc.*, **167**, 111506 (2020).
14. G. Šekularac, J. Kovač, and I. Milošev, *Corros. Sci.*, **169**, 108615 (2020).
15. M. Mujdrica Kim, B. Kapun, U. Tiringer, G. Šekularac, and I. Milošev, *Coatings*, **9**, 563 (2019).

16. F. Andreatta, A. Turco, I. de Graeve, H. Terryn, J. H. W. de Wit, and L. Fedrizzi, *Surf. Coat. Technol.*, **201**, 7668 (2007).
17. M. Mujdrica Kim, B. Kapun, and I. Milošev, *J. Electrochem. Soc.*, **172**, 061501 (2025).
18. G. Šekularac, J. Kovač, and I. Milošev, *J. Electrochem. Soc.*, **172**, 111501 (2025).
19. M. Ely, J. Światowska, A. Seyeux, S. Zanna, and P. Marcus, *J. Electrochem. Soc.*, **164**, C276 (2017).
20. A. Benninghoven, E. Niehuis, D. Greifendorf, D. van Leyen, and W. Lange, "Analytical Application of a High Performance TOF-SIMS." *Secondary Ion Mass Spectrometry SIMS* (Springer, Berlin, Heidelberg) Springer Series in Chemical Physics, 44, 497–499 (1986).
21. K. Wien, *Nucl. Instrum. Methods Phys. Res. B*, **131**, 38 (1997).
22. V. Cristaudo, K. Baert, P. Laha, M. Lyn Lim, E. Brown-Tseng, H. Terryn, and T. Hauffman, *Appl. Surf. Sci.*, **562**, 150166 (2021).
23. G. S. Frankel and M. Rohwerder, *Encyclopedia of Electrochemistry*, ed. M. Stratmann and G. S. Frankel Vol. 4(New York)(Wiley, Weinheim) (2003).
24. R. G. Kelly, J. R. Scully, D. Shoesmith, and R. G. Buchheit, *Electrochemical Techniques in Corrosion Science and Engineering* (Boca Raton, FL)(CRC Press, Boca Raton, FL) (2002).
25. F. D. Timmins and J. Oil, *Col. Chem. Assoc.*, **62**, 131 (1979).
26. J. B. Harrison and T. C. K. Tickle, *Journal of the Oil and Colour Chemists' Association*, **45**, 571 (1962).
27. R. L. Howard, S. B. Lyon, and J. D. Scantlebury, *Prog. Org. Coat.*, **37**, 91 (1999).
28. J. B. Harrison, *Br. Corros. J.*, **4**, 58 (1969).
29. ASTM International, *Standard Practice for Modified Salt Spray (Fog) Testing, ASTM G85-02, Annex A5* (ASTM International, West Conshohocken, PA) (2002).
30. G. Gusmano, G. Montesperelli, M. Rapone, G. Padeletti, A. Cusmà, S. Kaciulis, A. Mezzi, and R. D. Maggio, *Surf. Coat. Technol.*, **201**, 5822 (2007).
31. P. Rodič, I. Milošev, and G. S. Frankel, *J. Electrochem. Soc.*, **170**, 031503 (2023).
32. R. G. Buchheit, M. Cunningham, H. Jensen, M. W. Kendig, and M. A. Martinez, *Corrosion*, **54**, 61 (1998).
33. E. Barsoukov and J. R. Macdonald, *Impedance Spectroscopy*, ed. E. Barsoukov and J. R. Macdonald (New York)(Wiley, Hoboken, New Jersey) (2005).
34. J. M. Hu, J. Q. Zhang, and C. N. Cao, *Prog. Org. Coat.*, **46**, 273 (2003).
35. I. Milošev and G. S. Frankel, *J. Electrochem. Soc.*, **165**, C127 (2018).
36. M. Becker, *Corros. Rev.*, **37**, 321 (2019).
37. N. Birbilis and R. G. Buchheit, *J. Electrochem. Soc.*, **155**, C117 (2008).
38. Z. Jin, C. Cai, Y. Yuan, D. Kang, J. Hunter, and X. Zhou, *Mater. Charact.*, **171**, 110768 (2021).
39. Z. Jin, C. Cai, T. Hashimoto, Y. Yuan, D. Kang, J. Hunter, and X. Zhou, *Corros. Sci.*, **179**, 109134 (2021).
40. S. Verdier, S. Delalande, N. van der Laak, J. Metson, and F. Dalard, *Surf. Interface Anal.*, **37**, 509 (2005).
41. C. Pereira-Nabais, J. Światowska, A. Chagnes, F. Ozanam, A. Gohier, P. Tran-Van, C.-S. Cojocaru, M. Cassir, and P. Marcus, *Appl. Surf. Sci.*, **266**, 5 (2013).
42. J.-T. Li, V. Maurice, J. Swiatowska-Mrowiecka, A. Seyeux, S. Zanna, L. Klein, S.-G. Sun, and P. Marcus, *Electrochim. Acta*, **54**, 3700 (2009).
43. B. Díaz, J. Światowska, V. Maurice, A. Seyeux, B. Normand, E. Härkönen, M. Ritala, and P. Marcus, *Electrochim. Acta*, **56**, 10516 (2011).
44. B. Díaz, E. Härkönen, J. Światowska, V. Maurice, A. Seyeux, P. Marcus, and M. Ritala, *Corros. Sci.*, **53**, 2168 (2011).
45. J. Grams, *New Trends and Potentialities of ToF-SIMS in Surface Studies* (Nova Science Publishers) 273 (2007).
46. T. Sanchez, S. Zanna, A. Seyeux, M. Vaudescal, P. Marcus, P. Volovitch, and J. Światowska, *Appl. Surf. Sci.*, **556**, 149734 (2021).
47. M. Nabizadeh, K. Marcoen, E. A. Mernissi Cherigui, T. Kolberg, D. Schatz, H. Terryn, and T. Hauffman, *Surf. Coat. Technol.*, **441**, 128567 (2022).
48. R. C. Hiorns et al., *Pure Appl. Chem.*, **84**, 2167 (2012).
49. A. Ravve, *Principles of Polymer Chemistry* (Springer New York, New York, NY) (2012).
50. C. Walther, J. Rothe, M. Fuss, S. Büchner, S. Koltsov, and T. Bergmann, *in Analytical and Bioanalytical Chemistry*, **388**, 409 (2007).
51. T. Sasaki, O. Nakaoka, R. Arakawa, T. Kobayashi, I. Takagi, and H. Moriyama, *J. Nucl. Sci. Technol.*, **47**, 1211 (2010).
52. R. E. Connick and W. H. Reas, *J. Am. Chem. Soc.*, **73**, 1171 (1951).
53. A. Clearfield, *J. Mater. Res.*, **5**, 161 (1990).
54. D. B. Hibbert (ed.), *Compendium of Terminology in Analytical Chemistry* (The Royal Society of Chemistry) (2023).
55. C. Hagfeldt, V. Kessler, and I. Persson, *Dalton Trans.*, **14**, 2142 (2004).
56. P. D. Southon, J. R. Bartlett, J. L. Woolfrey, and B. Ben-Nissan, *Chem. Mater.*, **14**, 4313 (2002).
57. T. Kobayashi, S. Nakajima, R. Motokawa, D. Matsumura, T. Saito, and T. Sasaki, *Langmuir*, **35**, 7995 (2019).
58. T. Kobayashi, T. Fushimi, H. Mizukoshi, R. Motokawa, and T. Sasaki, *Langmuir*, **38**, 14656 (2022).
59. N. Rao, M. N. Holerca, and V. Pophristic, *J. Chem. Theory Comput.*, **4**, 145 (2008).
60. A. Kraš, Y. Wu, S. Lamaka, and I. Milošev, (2026), *To be submitted*.
61. O. Engler, K. Kuhnke, and J. Hasenclever, *J. Alloys Compd.*, **728**, 669 (2017).
62. D. G. Eskin, *Physical Metallurgy of Direct Chill Casting of Aluminum Alloys* (Boca Raton, FL)(CRC Press) (2008).
63. A. Afseth, J. H. Nordlien, G. M. Scamans, and K. Nisancioglu, *Corros. Sci.*, **43**, 2359 (2001).
64. *ГОСТ 9.302-88. Edinaya sistema zashchity ot korrozii i stareniya. Pokrytiya metallicheskie i nemetallicheskie neorganicheskie, Metodykontrolya* (Standardov, Moscow) (1990).
65. G. Greczynski and L. Hultman, *Prog. Mater Sci.*, **107**, 100591 (2020).
66. S. M. Lößlein, R. Merz, D. W. Müller, M. Kopnarski, and F. Mücklich, *Sci. Rep.*, **12**, 19389 (2022).
67. J. van den Brand, S. Van Gils, P. C. J. Beentjes, H. Terryn, and J. H. W. de Wit, *Appl. Surf. Sci.*, **235**, 465 (2004).
68. K. Siegbahn, C. L. A. Nordling, and A. Fahlman, *ESCA : Atomic, Molecular and Solid State Structure Studied by Means of Electron Spectroscopy*, ed. K. Siegbahn, C. L. A. Nordling, and A. Fahlman (Almqvist & Wiksells Boktryckeri AB, Uppsala) (1967).
69. J. P. B. van Dam, U. Tiringer, S. T. Abrahami, I. Milošev, H. Terryn, J. Kovač, and J. M. C. Mol, *Surf. Coat. Technol.*, **485**, 130901 (2024).
70. U. Tiringer, J. P. B. van Dam, S. T. Abrahami, H. Terryn, J. Kovač, I. Milošev, and J. M. C. Mol, *Surfaces and Interfaces*, **26**, 101417 (2021).
71. D. Chidambaram, C. R. Clayton, and G. P. Halada, *Electrochim. Acta*, **51**, 2862 (2006).
72. K. Ogle and M. Wolpers, "Phosphate Conversion Coatings." *Corrosion: Fundamentals, Testing, and Protection*, ed. S. D. Cramer and B. S. Covino (ASM International, Materials Park, OH)13A 712–719 (2003).
73. K. Ogle and R. G. Buchheit, "Corrosion and oxide films." *Encyclopedia of Electrochemistry*, ed. A. J. Bard and M. Stratmann (Wiley-VCH, Weinheim) Vol. 4 (2003).